

**Kelvin wave coupling from TIMED and GOCE
Inter/intra-annual variability and solar activity effects**

Gasparini, Federico; Forbes, Jeffrey M.; Doornbos, Eelco N.; Bruinsma, Sean L.

DOI

[10.1016/j.jastp.2017.08.034](https://doi.org/10.1016/j.jastp.2017.08.034)

Publication date

2018

Document Version

Final published version

Published in

Journal of Atmospheric and Solar - Terrestrial Physics

Citation (APA)

Gasparini, F., Forbes, J. M., Doornbos, E. N., & Bruinsma, S. L. (2018). Kelvin wave coupling from TIMED and GOCE: Inter/intra-annual variability and solar activity effects. *Journal of Atmospheric and Solar - Terrestrial Physics*, 171, 176-187. <https://doi.org/10.1016/j.jastp.2017.08.034>

Important note

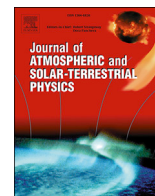
To cite this publication, please use the final published version (if applicable).
Please check the document version above.

Copyright

Other than for strictly personal use, it is not permitted to download, forward or distribute the text or part of it, without the consent of the author(s) and/or copyright holder(s), unless the work is under an open content license such as Creative Commons.

Takedown policy

Please contact us and provide details if you believe this document breaches copyrights.
We will remove access to the work immediately and investigate your claim.



Kelvin wave coupling from TIMED and GOCE: Inter/intra-annual variability and solar activity effects



Federico Gasperini^{a,*}, Jeffrey M. Forbes^b, Eelco N. Doornbos^c, Sean L. Bruinsma^d

^a Utah State University, Logan, UT, 87545, USA

^b University of Colorado at Boulder, Boulder, CO, 80302, USA

^c Delft University of Technology, Delft, The Netherlands

^d National Centre for Space Studies (CNES), Toulouse, France

ARTICLE INFO

Keywords:

Thermosphere wave coupling

DE3

UFKW

ABSTRACT

The primary mechanism through which energy and momentum are transferred from the lower atmosphere to the thermosphere is through the generation and propagation of atmospheric waves. It is becoming increasingly evident that a few waves from the tropical wave spectrum preferentially propagate into the thermosphere and contribute to modify satellite drag. Two of the more prominent and well-established tropical waves are Kelvin waves: the eastward-propagating 3-day ultra-fast Kelvin wave (UFKW) and the eastward-propagating diurnal tide with zonal wave number 3 (DE3). In this work, Sounding of the Atmosphere using Broadband Emission Radiometry (SABER) temperatures at 110 km and Gravity field and steady-state Ocean Circulation Explorer (GOCE) neutral densities and cross-track winds near 260 km are used to demonstrate vertical coupling in this height regime due to the UFKW and DE3. Significant inter- and intra-annual variability is found in DE3 and the UFKW, with evidence of latitudinal broadening and filtering of the latitude structures with height due to the effect of dissipation and mean winds. Additionally, anti-correlation between the vertical penetration of these waves to the middle thermosphere and solar activity level is established and explained through the effect of molecular dissipation.

1. Introduction

The middle (ca. 20–100 km) and upper (ca. > 100 km) atmosphere of Earth is a highly coupled system, where processes at one height strongly influence processes at other heights. Vertically-propagating waves in the mesosphere-lower-thermosphere (MLT) region (ca. 80–150 km) determines much of the dynamics of this region and of the middle to upper thermosphere due to the filtering of upward propagating disturbances. When a global-scale wave with sufficiently large amplitude and long wavelength propagates into the E-region ionosphere (ca. 100–150 km), it drives electric fields and currents at the period of the global-scale wave, through the dynamo action of tidal winds. The electric fields map along equipotential magnetic lines and drive $E \times B$ plasma drifts in the F-region, which cause the temporal and spatial variability of the E-region tides to transfer to the F-region plasma [e.g. Jin et al., 2008; Kil et al., 2007, 2008; Liu et al., 2007; Liu and Watanabe, 2008]. The vertical propagation of some of these wave components to the upper thermosphere [300–400 km; Forbes et al., 2009; Forbes et al., 2014; Hagan et al., 2009]

also directly modulate neutral and plasma densities [He et al., 2011; England et al., 2010]. These waves represent the primary mechanism through which energy and momentum are transferred from the lower atmosphere to the thermosphere and ionosphere. Variability associated with these waves competes with other meteorological influences, geomagnetic activity, and solar flux changes to produce ionospheric variability that undermines operation of various communications and navigation systems, and neutral density variability that contributes significantly to uncertainty in satellite orbit and reentry predictions.

Atmospheric waves are periodic in both time and longitude and can individually be expressed in the form $A_{s\delta} \cos(\delta\Omega t + s\lambda - \Phi_{s\delta})$, where $A_{s\delta}$ and $\Phi_{s\delta}$ are the amplitude and phase of the oscillation (both functions of latitude and height), t = time, λ = longitude, Ω = Earth's rotation rate ($2\pi/24$ hrs), δ defines the wave frequency, and the zonal wavenumber (s) specifies the wave's periodicity in longitude. In this notation the frequency is taken to be positive and $s < 0$ ($s > 0$) corresponds to eastward (westward) wave propagation. Integer values of δ (1, 2, 3) correspond to diurnal, semidiurnal and terdiurnal tides, with periods of 24, 12 and 8 h,

* Corresponding author.

E-mail address: gasperini@usu.edu (F. Gasperini).

respectively. Values of $\delta < 1$ correspond to wave periods greater than a day.

The efficiency with which a given wave is excited depends upon how well that wave projects onto the spatial and temporal variability of the forcing. In the tropical troposphere, a whole spectrum of equatorially-trapped waves are generated as the result of variable convective activity and associated latent heat release: Kelvin waves, mixed Rossby-Gravity waves, diurnal and semidiurnal tides, equatorial Rossby waves. These waves capture much of the longitude-latitude and temporal response of the atmosphere to this variable forcing, which is moreover modulated on both intra-annual (e.g., 20–60 day Madden-Julian Oscillation, MJO) and inter-annual (e.g., El Niño Southern Oscillation, ENSO) time scales. The efficiency with which a given wave propagates into the thermosphere system depends on its period and vertical wavelength, the shorter-period and longer-wavelength waves being less affected by dissipation and therefore being more capable of propagating to high altitudes [Forbes and Garrett, 1979].

It is becoming increasingly evident that a few waves from the tropical wave spectrum preferentially propagate into the thermosphere [e.g., Forbes et al., 2009; Oberheide et al., 2009], and modify satellite drag, causing in-track prediction differences of order 200 ± 100 m for satellites in 400-km circular orbits for a 24-hour prediction [Leonard et al., 2012]. Two of the more prominent and well-established tropical waves are the eastward-propagating 2–3-day period ultra-fast Kelvin wave with zonal wave number $s = -1$ (UFKW) and the eastward-propagating diurnal tide with zonal wave number $s = 3$ (DE3) [Gasperini et al., 2015]. Kelvin waves are one of the PW types trapped in the equatorial and low-latitude region where the Coriolis force is negligible, and are considered a special kind of gravity wave modified by the Earth's rotation [Andrews et al., 1987]. Kelvin waves are eastward propagating waves and have predominance of the kinetic energy in the zonal wind component. UFKW, first reported in the MLT by Salby et al. (1984), have the longest vertical wavelength (>50 km) among all Kelvin waves and thus can penetrate well into the lower thermosphere, reaching amplitudes of 25 K in temperature and 30 m/s in zonal wind [Gu et al., 2014], and into the middle thermosphere [Gasperini et al., 2015]. DE3 is a large source of variability in the MLT and is sometimes the single largest tidal component above the mesopause [Forbes et al., 2008; Oberheide and Forbes, 2008; Mukhtarov and Pancheva, 2011; Pancheva and Mukhtarov, 2010], and the main sources of the longitudinal wave number 4 structure in the ionosphere [Immel et al., 2006]. Its first and largest mode is a Kelvin wave (i.e., symmetric about the equator with relatively small meridional wind velocity, see Forbes et al., 2003 and Truskowski et al., 2014) that is known to propagate higher into the thermosphere due to its vertical wavelength of ~ 56 km [Oberheide et al., 2011; Forbes et al., 2014]. Dissipation of DE3 accelerates, heats, and mixes the composition of the thermosphere (e.g., Jones et al., 2014).

By analogy with the need to understand conditions on the Sun that translate to solar-driven space weather, it is also important to understand the sources and propagation conditions that make possible for a set of tropospheric waves to propagate well into the thermosphere. However, relatively little is known about how background atmospheric conditions filter the tropical wave spectrum and modulate it into the thermosphere. Additionally, the observational database to elucidate the connection between lower and middle thermosphere waves is very limited because global satellite-borne observations of the neutral dynamics exist between ~ 120 km and ~ 260 km are sparse. Addressing this issue is important to understanding what might be involved in achieving a predictive capability that connects tropical tropospheric weather with IT space weather, and what priorities might be placed on pursuing such a capability. One approach to obtain observation-based tidal fields in this ‘thermospheric gap’, as defined by Oberheide et al., 2011, has been constraining a physics-based empirical model with tidal observations made in the mesosphere-lower-thermosphere (MLT) region [e.g., Forbes et al., 2009; Oberheide et al., 2009, 2011]. Recently, García-Comas et al., 2016 utilized Michelson Interferometer for Passive Atmospheric Sounding

(MIPAS) temperature measurements at two fixed local times from 120 to 170 km to derive pole-to-pole estimates of odd tidal frequencies. These authors suggested that MIPAS global measurements of longitudinal oscillations could be used for testing thermospheric tidal models and to set lower boundary conditions in present models.

Gasperini et al., 2015 have developed and applied techniques to satellite data sets to reveal short-term variability in the thermosphere directly attributable to DE3 and UFKW. These authors demonstrate that DE3 and UFKW propagate from 100 km to 260 km on daily and monthly time scales, and that through nonlinear interaction produce secondary waves that do the same. They found that for low to moderate solar and geomagnetic conditions, the combined effect of DE3, the UFKW, and their interactions account for 20%–60% of the low-latitude variability, while only up to 40% of the variability is ascribable to geomagnetic and solar effects. Gasperini et al., 2015 showed that the majority (about 60%) of the variance in DE3 and the UFKW at 260 km can be traced back to variability occurring at 100 km, but also conjectured that the significant differences observed in the latitude-temporal structures between the two heights are likely introduced by the effect of wave dissipation, the presence of zonal mean winds, wave-wave interactions, and inherent transience.

This paper examines the seasonal and interannual variability of DE3 and UFKW and investigates the effect of solar activity on the vertical propagation of these two tropospheric wave components from the lower (i.e., 110 km) to the middle (i.e., 260 km) thermosphere. In section 2, we provide a description of the dataset (i.e., quasi-Sunsynchronous satellite measurements) and method used to study the evolution of wave amplitudes on a daily basis. In section 3, we present evidence of vertical propagation of DE3 and the UFKW between the lower and middle thermosphere and their day-to-day variability (section 3.1), longer time-scale (i.e., intra-annual and interannual) variations (section 3.2), and the effect of solar EUV radiation on the vertical propagation from 110 km to 260 km (section 3.3). The summary of our findings and conclusions are then presented in section 4.

2. Data and methodology

Satellite observations are a crucial component of research into the coupling processes that link the upper atmosphere to the lower atmosphere and provide a unique perspective due to their sampling patterns (i.e., spatially global but temporally asynoptic). In this work we employ global temperatures (version v2.0) at 110 km from the Sounding of the Atmosphere using Broadband Emission Radiometry (SABER) instrument aboard the Thermosphere, Ionosphere, Mesosphere, Energetics and Dynamics (TIMED) satellite, and neutral densities and winds (version v1.5) at 260 km derived from accelerometer measurements taken by the Gravity field and steady-state Ocean Circulation Explorer (GOCE) satellite. The analysis is performed during the 3-year period between 1 January 2010 and 31 December 2012 at low-to mid-latitudes ($\pm 45^\circ$), where DE3 and the UFKW reach their largest amplitudes and sampling is not affected by yaw maneuvers for TIMED.

The SABER instrument was launched onboard the TIMED satellite on 7 December 2001. Among other parameters, SABER provides measurements of kinetic temperature from approximately 20 km–120 km altitude, during both day and night, and extending to latitudes as high as $\pm 82^\circ$ with close to 100% duty cycle. SABER views the atmosphere 90° to the satellite velocity vector in a 625 km and 73° inclination orbit so that latitude coverage on a given day extends from about 53° latitude in one hemisphere to 83° in the other. This viewing geometry alternates once every 60 days due to 180° yaw maneuvers required for the TIMED satellite. This type of coverage provides unprecedented opportunities for the study of tides and planetary waves, and their roles in coupling the troposphere, stratosphere, mesosphere, and thermosphere. As noted by Zhang et al., 2006, unmodeled atomic oxygen variations can also introduce errors into the retrieved temperatures. For this reason results above ~ 110 km contain errors of unknown magnitude and are avoided for

this study.

GOCE was launched on 17 March 2009 into a near-circular and quasi-Sun-synchronous orbit ($i = 96.5^\circ$) at around 270 km, and remained in orbit until 10 November 2013. GOCE was the first European Space Agency (ESA) Earth-Explorer core mission [Drinkwater et al., 2003]. The objective of the mission was high-resolution mapping of the gravity field of the Earth, to which end GOCE was equipped with an ensemble of six three-axis accelerometers constituting the main part of the gravity gradiometer instrument. GOCE provided a total mass density and wind product different than that of CHAMP due to the spacecraft's lower altitude (260 km versus 400 km) and dawn-dusk orbit. The nearly constant altitude and local solar time over each measurement phase made the GOCE mission profile particularly interesting for upper atmosphere studies, i.e., seasonal and solar cycle variations are not mixed with local time variations (this comes at the cost of local time coverage). Neutral densities were derived from GOCE using ion thruster data combined with accelerometer and star camera data products. Using the satellite area, orientation, and modeling of radiation pressure, total mass density along the satellite orbit, and winds orthogonal to the orbit were inferred from the accelerometer data and thruster accelerations [Bruinsma et al., 2013; Bruinsma et al., 2014; Doornbos 2016; Doornbos et al., 2013, 2014]. This involved iterative adjustment of wind direction and density inputs of an aerodynamic model of the satellite until the modeled aerodynamic accelerations matched the observations. The largest error sources in the GOCE density derivation are the gas-surface interaction, modeling of the satellite geometry, the calibration scale factor for the in-track accelerometer component, and the knowledge of the atmospheric in-track wind speed, composition and temperature. The dominant source of errors in the crosswind data are due to acceleration errors in the spacecraft body-fixed Y-direction. These errors are mainly due to accelerometer biases, radiation pressure variability, and thruster activations. The level of these acceleration errors with respect to the aerodynamic acceleration determines the level of crosswind error. GOCE's low orbit, where aerodynamic accelerations are very strong, is therefore a big advantage for obtaining high accuracy crosswind data. The current work utilizes density and wind data from GOCE extending from 1 January 2010 to 31 December 2012. During this time GOCE was in a near-circular orbit at a mean altitude of 260 km, until mid-2012 when a series of orbit adjustments were performed to lower the mean altitude to 250 km in August 2012, to 245 km in November 2012. During this period the local time of GOCE's orbit slowly drifted from 0600/1800 to 0730/1930 LT. Measurement errors decreased throughout the analysis period, especially after the orbit adjustments to lower altitudes. Density (wind) errors decreased on average from about 2.5% (30–40 m/s) during 2009–2010 to 1.5% (15–20 m/s) until August 2012 and then remained around 1% (7–12 m/s) until November 2013. The main source of errors is noise due to ion thruster and radiation pressure modeling errors, which translates to errors in wave amplitudes of unknown magnitude (a comprehensive analysis on this issue has not been performed yet). See Doornbos et al., 2014 and Doornbos 2016 for more information on the derivation method and related errors.

In order to highlight the thermosphere variability associated with waves, we use multiple linear regression to fit the raw data to daily S10.7 and 3-hour ap values in 15-day windows, stepping forward 1 day at a time ('running windows'). We then remove these fits from the raw data and analyze the resulting residuals for wave content. S10.7 has been shown to be better proxy for EUV variability than the commonly used F10.7 solar flux, especially for day-to-day variations during solar low conditions [Tobiska et al., 2008]. S10.7 is derived by normalizing and converting to solar flux units (SFU) through linear regression with F10.7 measurements of the 26–34 nm solar EUV emission from the Solar Extreme-ultraviolet Monitor instrument aboard the NASA/ESA Solar and Heliospheric Observatory research satellite [Bowman et al., 2008].

The slow local time precession of most low-orbiting satellites represents a major limitation of utilizing satellite-based measurements to analyze the short-term variability of atmospheric tides, such that only

tidal fields averaged over 60 days or more can be retrieved. To counteract this shortcoming, this study employs a similar method to that of Lieberman 1991 and Oberheide and Gusev 2002 to SABER and GOCE residuals (i.e., data after the removal of ap-S10.7 fits) to infer 'daily' DE3 amplitudes. The method, which involves taking differences between measurements at the ascending and descending nodes and least-squares fitting wave-4, was first formulated by Hitchman and Leovy 1985. Lieberman 1991 and Oberheide et al., 2000 demonstrated that amplitude and phase of DW1 could be estimated from the vertical structure of the zonal mean component of the ascending-descending difference pattern. Oberheide et al., 2000 also discussed the complexities associated with the recovery of nonmigrating tides using this method. A diurnal tide with zonal wave number s is viewed by the satellite as a stationary zonal wave number $k_s = s - 1$ for westward propagation and $k_s = s + 1$ if eastward propagating. Thus, an integer-valued k_s in an ascending-descending node spectrum represents the juxtaposition of a westward propagating diurnal tide with $s = k_s + 1$ and an eastward propagating diurnal tide with $m = k_s - 1$. Below a brief overview of the mathematical formulation for this method is presented.

A tidal component with period n/Ω can be represented as $A_{n,s} \cos(n\Omega t + (s - n)\lambda - \phi_{n,s})$. Thus, following the example of Oberheide et al., 2011, from the ascending (descending) leg of a satellite measures the tidal component at local time t_A (t_D) one can write

$$A = A_{n,s} \cos(n\Omega t_A + (s - n)\lambda - \phi_{n,s}) \quad (1)$$

and

$$D = A_{n,s} \cos(n\Omega t_D + (s - n)\lambda - \phi_{n,s}) \quad (2)$$

thus, using the sum-to-product trigonometric identities

$$\cos A - \cos B = -2 \sin[(A + B)/2] \sin[(A - B)/2] \quad (3)$$

and

$$\cos A + \cos B = 2 \cos[(A + B)/2] \cos[(A - B)/2] \quad (4)$$

one can write

$$\frac{A - D}{2} = -A_{n,s} \sin\left(n\Omega \frac{t_A - t_D}{2}\right) \sin\left(n\Omega \frac{t_A + t_D}{2} + (s - n)\lambda - \phi_{n,s}\right) \quad (5)$$

Since at low-mid latitudes most satellites (e.g., TIMED and GOCE) satisfy the relationship

$$(t_A - t_D)/2 = \pm 12 \text{ hr} \quad (6)$$

and so

$$n\Omega(t_A - t_D)/2 \approx \pi/2, \quad (7)$$

the previous expressions can be written as

$$\frac{A - D}{2} \approx \mp A_{n,s} \sin\left(n\Omega \frac{t_A + t_D}{2} + (s - n)\lambda - \phi_{n,s}\right) \quad (8)$$

Hence, each day (for ~ 14 orbits/longitudes), we can fit wave $s - n$ in $(A - D)/2$ and $(A + D)/2$ to get the amplitude $A_{n,s} = A'$ and phase $\phi_{n,s} = \phi' + n\Omega(t_A + t_D)/2$ of a tidal component on a daily basis. The daily resolution is very valuable, but the main shortcoming as previously mentioned is that waves with the same $s - n$ alias into each other, and hence cannot be distinguished. For instance, when estimating DE3 from wave 4 ($s - n = 4$) of ascending minus descending differences the main source of error is represented by aliasing of TE1 and DW5, which cause uncertainties ranging from $\sim 5\%$ during the Northern Hemisphere summer to $\sim 30\%$ during the Northern Hemisphere winter at low latitudes

and altitudes of ~ 100 km (according to Oberheide et al., 2011). Another drawback to this technique is that semidiurnal tidal components can alias into the diurnal tidal estimates, when the ascending and descending nodes are not exactly 12 h apart. The difference in local time between the equatorial ascending and descending nodes is about 9 h for SABER (i.e., $(t_A - t_D)/2 = \pm 9hr$). For the diurnal tide ($n = 1$) $\sin(\Omega(t_A - t_D)/2) \approx 0.92$ while for the semidiurnal tide ($n = 2$) $\sin(2*\Omega(t_A - t_D)/2) \approx 0.71$, thus a $\sim 8\%$ amplitude reduction and a 71% SE2 aliasing can be expected due to the 9-hr local time difference. Note that low-latitude SE2 amplitudes are very small (up to $\sim 3K$, see, e.g., Truskowski et al., 2014). Overall, DE3 amplitudes extracted with the method presented above are expected to possess an uncertainty of 5–10% for GOCE and 10–20% for SABER. This method, successfully used by Gasperini et al., 2015 to extract DE3 amplitudes from SABER and GOCE data on a day-to-day basis, is implemented using 5-day running means. We find this averaging necessary based on the noise level on the raw data. In the following, we refer to these DE3 values as ‘daily’ amplitudes, although the reader should keep in mind that these values are actually 5-day means.

3. Results

3.1. Evidence of vertical propagation

Fig. 1 shows the period vs. zonal wavenumber spectrum for

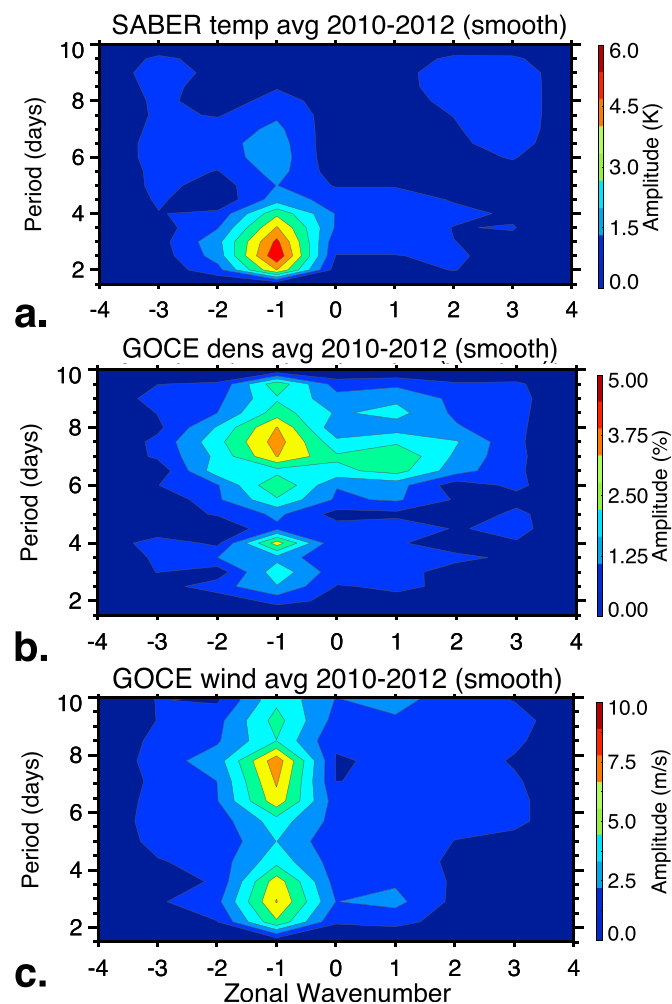


Fig. 1. Three-year average period vs. zonal wavenumber spectrum, with ap/S10.7 fits removed, after the repeated 1-2-1 smoothing to the original spectrum is removed from the original spectrum for SABER temperature (panel a), GOCE density (panel b), and GOCE wind (panel c). Note a strong 3-day UFKW at both 110 and 260 km, and 6–9 day Kelvin waves at 260 km.

2010–2012 around the equator ($\pm 12^\circ$ latitude), produced by least-squares fitting the residuals after removing ap-S10.7 effects. The multi-year spectrum of Fig. 1 has the ‘background energy’, obtained by repeated 1-2-1 smoothing to the original spectrum, removed from the original spectrum. This method is the same that Wheeler and Kiladis 1999 applied to outgoing longwave radiation (OLR) data in the tropics to highlight several convectively-generated waves, and that Forbes et al., 2009 applied to SABER temperatures to reveal Kelvin waves and other equatorial oscillations over the altitude range 20–120 km. Fig. 1 presents evidence of a strong 3-day UFKW with $s = -1$ in SABER temperature (panel a), and Kelvin waves ($s = -1$) with periods ranging from 3 to 9 days in GOCE density (panel b) and GOCE wind (panel c). The 3-year average UFKW amplitude is ~ 5 K in SABER temperature, and $\sim 4\%$ and ~ 7 m/s in GOCE density and wind, respectively. Note that the 6–9 day Kelvin waves present in GOCE data are not found in SABER, suggesting that these thermospheric oscillations arise from in-situ excitation, possibly due to secondary waves generated by nonlinear wave-wave interactions and/or interactions with the longitudinal structure of ion drag (i.e., magnetic control of ion-neutral interactions, see Jones et al., 2013). It would be beyond the scope of the present study to further investigate the origin and nature of these oscillations present at 260 km, but not at 110 km; thus this analysis is left for future work. Note that Gasperini et al., 2015 showed evidence of a large 10-day periodicity with zonal wavenumber 0 both at 110 km and 260 km for the year 2011. This oscillation was significantly reduced in the spectrum after these authors removed ap-F10.7 fits, suggesting a link to geomagnetic and solar effects. In fact, this periodicity is likely related to recurrent geomagnetic activity due to high-speed solar wind streams near 9-day period, the signatures of which have been reported in both TIMED temperature data near 110 km [Jiang et al., 2014] and CHAMP density data near 400 km [Lei et al., 2008]. Note that this periodicity is not present in the 3-year average spectrum displayed in Fig. 1.

Fig. 2 shows daily DE3 amplitudes in SABER temperatures at 110 km (Fig. 2a) and GOCE densities (Fig. 2b) and winds (Fig. 2c) at 260 km for 2010–2012. Amplitudes up to 20 K are found in the temperatures, 8% in the densities, and 10 m/s in the winds. Note that the DE3 density perturbations from SABER are larger than those reported by Oberheide and Forbes 2008 (by a factor of 4), likely due to amplitude reduction caused the 60-day running means (see e.g., Häusler et al., 2015 and errors in extracting tidal fields with Hough Mode Extensions (HMEs; see the following subsection for more details on HMEs). The intraseasonal variability of DE3 is very similar at 110 km and 260 km, with maxima at low latitudes. The presence of DE3 at both heights, the common intraseasonal variability, and the similar amplitudes are a clear indication that vertical propagation is occurring. In addition we do not know of any source for DE3 between 110 km and 260 km. The correlation coefficients between SABER temperature and GOCE density is 0.67 for daily values and 0.73 for the 30-day running means (see Table 1). No link with season, level of geomagnetic activity, or zonal mean winds is found. Generally (see Truskowski et al., 2014 and references therein), DE3 tends to have a symmetric latitudinal structure with maxima around the equator due to the prevalence of its first symmetric mode, i.e., Kelvin wave symmetric about the equator. The presence of other Hough modes, such as the first anti-symmetric mode, can alter such symmetric structure and give rise to maxima at low latitudes, instead of the equator [Forbes et al., 2003]. This is likely the cause of the low-latitude non-equatorial peaks, particularly evident at 110 km (see Fig. 2a). While many similarities between the two heights are evident in the temporal evolution of the maxima, the latitudinal structures at 260 km are broader than those at 110 km. This latitudinal spread is a feature imposed by molecular dissipation (see Forbes and Hagan 1982 and Forbes and Vincent 1989 for the analytic theory).

As previously discussed, after the removal of the ap-S10.7 fits from the raw data the UFKW with 3-day period emerges as a prevalent short-period global wave both at 110 km and 260 km. Fig. 3 shows daily UFKW amplitudes for GOCE at 260 km and SABER at 110 km. UFKW amplitudes

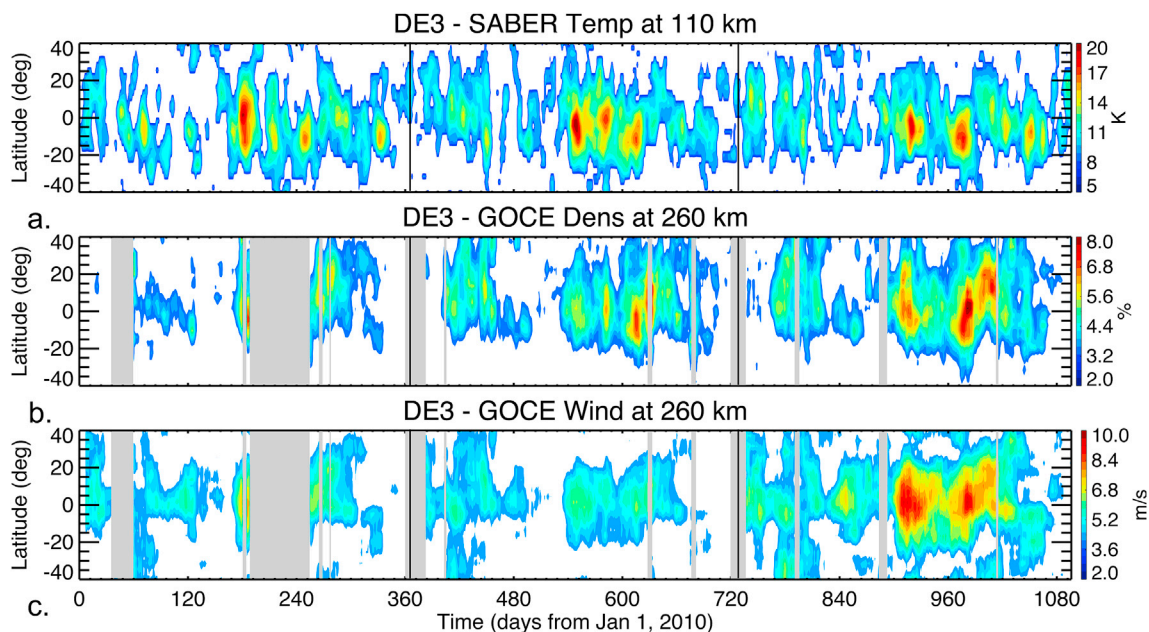


Fig. 2. Time series of daily DE3 amplitudes for SABER temperature (panel a), GOCE density (panel b), and GOCE wind (panel c) for 2010–2012. Large day-to-day and seasonal variability at both heights is present, with low-latitude maxima. Amplitudes up to 20 K are found in the temperatures, 8% in the densities, and 10 m/s in the winds. Based on the noise level in the extracted DE3 amplitudes, values smaller than 5 K, 2%, 2 m/s are not shown (white spaces), while gaps in the raw data are colored in gray. The similar intra- and inter-seasonal variability and amplitudes, and the absence of any known source for DE3 between 110 km and 260 km, is clear indication of the vertical propagation of DE3 from 110 km to 260 km.

Table 1

Correlation coefficients of daily and monthly DE3 in SABER temperature, GOCE density, and GOCE wind, calculated around the equator ($\pm 12^\circ$ latitude) for 2010–2012.

Correlation	DE3 Daily	DE3 Monthly
Temperature and Density	0.67	0.73
Density and Wind	0.81	0.84
Temperature and Wind	0.63	0.71

are derived by least-squares fitting residuals in 15-day running windows (15-day means shifted 1 day at the time), using the expression $y(t, \lambda) = \bar{y} + A \cos[2\pi(t/T - \lambda m)]$, where t is UT time, λ is longitude (in

radians), \bar{y} is the zonal mean, A the amplitude, T the period (i.e., 3 days), and m the zonal wavenumber (i.e., -1). The length of the window is chosen such that at least 5 full cycles are required to fully capture a wave with a 3-day period. Amplitudes up to 15 K are found in the temperatures (Fig. 3a), 8% in the densities (Fig. 3b), and 10 m/s in the winds (Fig. 3c), with maxima around the equator. The common intra-seasonal variability of the latitude-time amplitude structures between SABER and GOCE, and the absence of any known UFKW source between 110 km and 260 km, is indication that vertical propagation is occurring. Table 2 lists the correlation coefficients between the UFKW in SABER and GOCE. Correlation coefficients of 0.61 for daily values and 0.70 for running means are found between UFKW temperatures at 260 km and UFKW densities at 110 km.

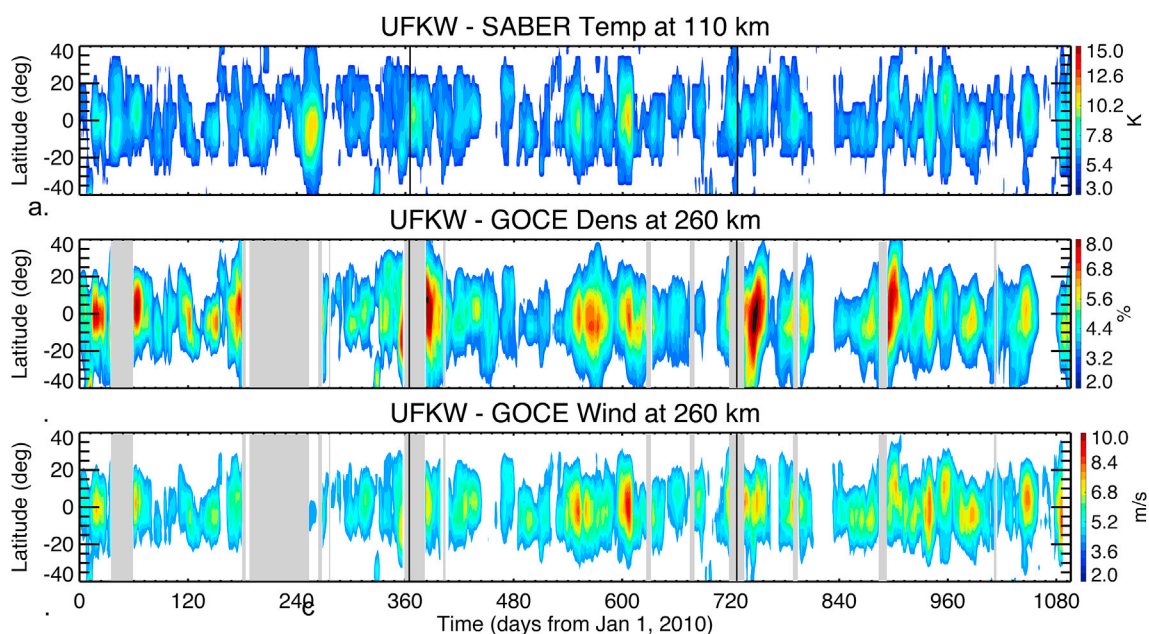


Fig. 3. Same as Fig. 2, but for the UFKW with period of 3 days and zonal wavenumber -1 . Amplitudes up to 15 K are found in the temperatures (panel a), 8% in the densities (panel b), and 10 m/s in the winds (panel c), with maxima at low latitudes.

Table 2

Correlation coefficients between different years for DE3 in SABER temperature at 110 km and GOCE density 260 km. This table refers to daily amplitudes and is calculated around the equator ($\pm 12^\circ$ latitude). Note values greater than 0.7 for SABER and 0.6 for GOCE, indicating strong year-to-year repeatability.

Correlation for DE3	SABER temperature	GOCE density
2010–2011	0.75	0.61
2010–2012	0.71	0.63
2011–2012	0.74	0.69

Similar to DE3, the latitude structures of UFKW amplitudes are broader at 260 km than those at 110 km, likely owing to the effect of dissipation.

3.2. Seasonal and inter-annual variability

Comparing the latitude-temporal variability of DE3 and UFKW structures for different years, one can investigate the extent to which this variability repeats from year to year. Significant repeatability for the salient features of DE3 is found at both 110 km and 260 km. Correlation coefficients between different years calculated around the equator ($\pm 12^\circ$ latitude) are reported in Table 3. As listed in Table 3, correlation coefficients greater than 0.7 and 0.6 are found at 110 km and 260 km, respectively. This level of correlation is evidence of significant year-to-year repeatability, but also indication of some degree of interannual variability. Interannual variations are not unexpected and can be explained by variability in tropospheric forcing (i.e., latent heat release) and propagation conditions (i.e., changes in zonal mean winds and dissipation conditions). Changing mean winds in the 110–260 km height region would also explain less year-to-year coherence at 260 km than at 110 km. Table 4 lists the correlation coefficients between different years of daily UFKW amplitudes. Values smaller than 0.56 are found at both 110 km and 260 km, indicating some year-to-year repeatability, but also significant interannual variability. Similar to DE3 (Table 3), the correlation coefficients at 260 km are smaller than those at 110 km, and may be explained by interannual variations in zonal mean winds between 110 km and 260 km that can increase (i.e., eastward zonal mean winds) or decrease (i.e., westward zonal mean winds) susceptibility to dissipation, resulting in less year to year coherence at 260 km than at 110 km. Additionally, Table 4 indicates that the UFKW has less annual repeatability than DE3, with correlation coefficients up to 0.75 for latter and only 0.54 for the former. The exact reasons of this difference are not known, although variations in year-to-year forcing and zonal mean wind effects for the two waves are the likely cause.

In addition to strong interannual variability, DE3 and UFKW also show significant seasonal variations. Fig. 4 (Fig. 5) presents the latitude-temporal evolution of DE3 (UFKW) amplitudes at 110 km and 260 km obtained combining data for the 3 years. Averaging 3 years of data shows the variability that repeats from year to year, and thus highlights seasonal patterns. The amplitudes and phases are computed in 5-day intervals

Table 3

Same as Table 1, but for the UFKW. Note correlation coefficients of 0.70 (0.67) between temperatures and densities (winds) for the 30-day means.

Correlation	UFKW Daily	UFKW Monthly
Temperature and Density	0.61	0.70
Density and Wind	0.79	0.86
Temperature and Wind	0.59	0.67

Table 4

Same as Table 2, but for the UFKW. Note values greater than 0.5 for SABER and GOCE, indicating some year-to-year repeatability, but also significant interannual variability.

Correlation for UFKW	SABER temperature	GOCE density
2010–2011	0.54	0.51
2010–2012	0.56	0.49
2011–2012	0.51	0.53

moved forward 1 day at the time and are then averaged over the 3 years on a daily basis. As shown in Fig. 4, the seasonal course of DE3 at both 110 km and 260 km is dominated by an annual oscillation with maxima between DOY 170 and DOY 300. The largest DE3 amplitudes, observed around DOY 170–200 and DOY 240–260, are ~ 16 K at 110 km and ~ 10 m/s ($\sim 6\%$) at 260 km, while those of the secondary amplification around DOY 20–120 are ~ 8 K at 110 km and ~ 6 m/s ($\sim 3\%$) at 260 km. On average, summer (DOY 170–265) DE3 amplitudes in the southern hemisphere are slightly larger than those in the northern hemisphere. Signatures of a semi-annual oscillation can be distinguished, with maxima around DOY 20–140 and DOY 170–300. The seasonal variability in DE3 outlined above is similar to what is reported by Truskowski et al., 2014 and Forbes et al., 2014. Forbes et al., 2014 exploited the local time coverage offered by combining CHAMP and GRACE data together and derived tides in terms of 72-day mean values. As discussed earlier, previous tidal analyses with CHAMP were performed in terms of perturbation density and consisted of 130-day mean values due to the slow local time precession of the CHAMP orbit, likely suppressing the amplitudes and significantly smearing month-to-month variability. In this study, we further reduced the amplitude suppression by looking at 5-day means. As a result, the temporal resolution attained reveals much more intra-seasonal variability in DE3, as shown in Fig. 4, than shown in most studies employing satellite observations [e.g., Forbes et al., 2014] [Note that Gasperini et al., 2015 already showed day-to-day variability of DE3 and UFKW, but was limited to the year 2011.]. Fig. 5 presents UFKW amplitudes, vector averaged over 2010–2012, for SABER and GOCE in a latitude versus DOY format. The UFKW shows a very distinct semi-annual variation at 260 km, with maxima of $\sim 4\%$ and ~ 6 m/s around DOY 1–60 and DOY 170–260. A less defined seasonal pattern can be seen at 110 km, where maxima of 6–7 K are found throughout the year. This seasonal modulation of the UFKW at 260 km, not present at 110 km, ought to be explained by the effect of dissipation and zonal mean winds acting between 110 km and 260 km.

Summarizing the results shown in Figs. 4 and 5, we found that: (1) DE3 maximizes within about $\pm 15^\circ$ latitude both at 110 km and 260 km, and can be detected in the $\pm 30^\circ$ latitude range, while the UFKW maximizes within about $\pm 25^\circ$ latitude at 110 km and possesses non-negligible amplitudes up to $\pm 40^\circ$ latitude at 260 km. Latitudinal asymmetries and non-equatorial maxima for DE3 and the UFKW represent departures from HME solutions (see Oberheide et al., 2011 for the first symmetric mode of DE3 and Forbes [2000] for the UFKW) and can be explained by the effect of zonal mean winds; (2) while the seasonal course of the DE3 tide is dominated by strong maxima around DOY 170–300 and secondary maxima around DOY 20–120 both in the lower and middle thermosphere, the UFKW shows weak seasonal dependence at 110 km but a strong semi-annual oscillation at 260 km, possibly introduced by the intervening wind field; (3) significant latitudinal asymmetry is found in both DE3 and the UFKW, which is likely associated with the combined effect of dissipation and zonal mean winds.

3.3. Solar activity effects on the vertical propagation

3.3.1. Review of the processes

Although the solar cycle dependence of upward-propagating tides is clearly established both theoretically and observationally [Lindzen and McKenzie, 1967; Forbes and Garrett, 1979; Oberheide et al., 2009], before we proceed the processes involved warrant some clarification.

Above about 100 km, molecular diffusion is the dominant dissipation mechanism for vertically-propagating waves. Exponential growth of a vertically-propagating wave ceases (i.e., peak occurs) when the time scale for molecular dissipation is of order the wave period [Chapman and

Lindzen, 1970] $\chi = \left| \frac{2\pi}{\lambda} \frac{\mu_0}{\rho} \frac{1}{\sigma} \right| \approx 1$, where λ is vertical wavelength of the wave, μ_0 is the molecular dissipation coefficient, ρ_0 is mean density, and σ is the frequency of the wave. When $\chi \sim 1$ dissipation is considered

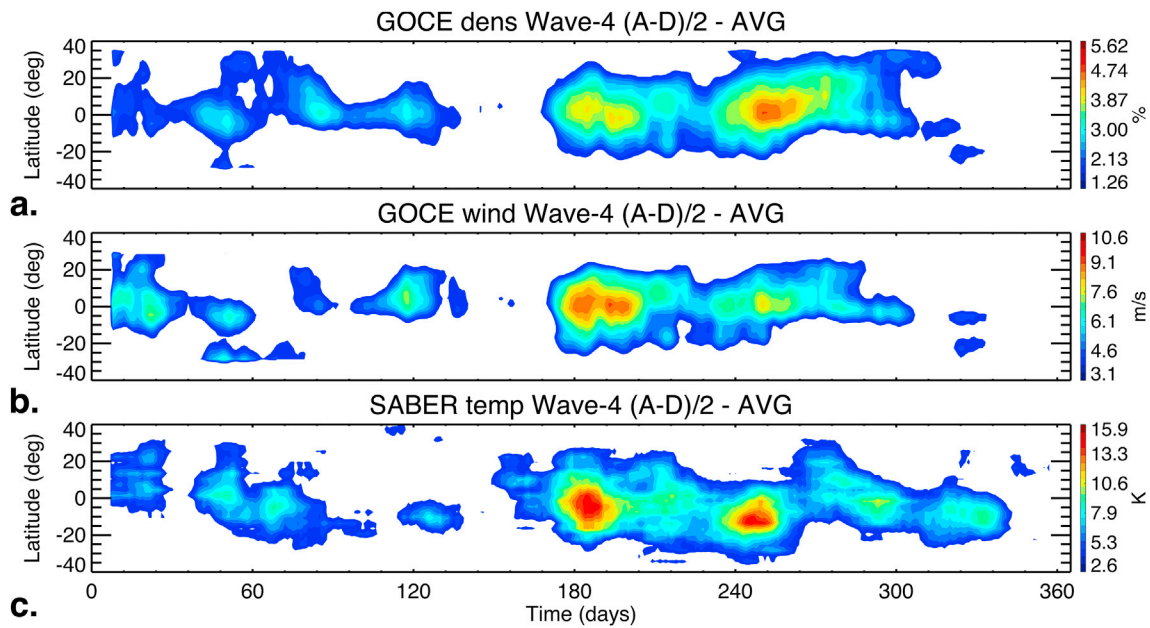


Fig. 4. Comparison between DE3 in GOCE density and wind (panels a and b), and DE3 in SABER temperature (panel c), obtained by combining 3-year of data before the fit with wave-4. Significant seasonal variability in DE3 at both 110 km and 260 km, with the largest DE3 amplitudes (6%, 10 m/s, 16 K) observed at DOY 170–200 and DOY 240–260 and a secondary amplification at DOY 20–120 (3%, 6 m/s, 8 K). Amplitudes smaller than 2.6 K, 3.1 m/s, 1.26%, based on the noise level on the raw data, are not plotted.

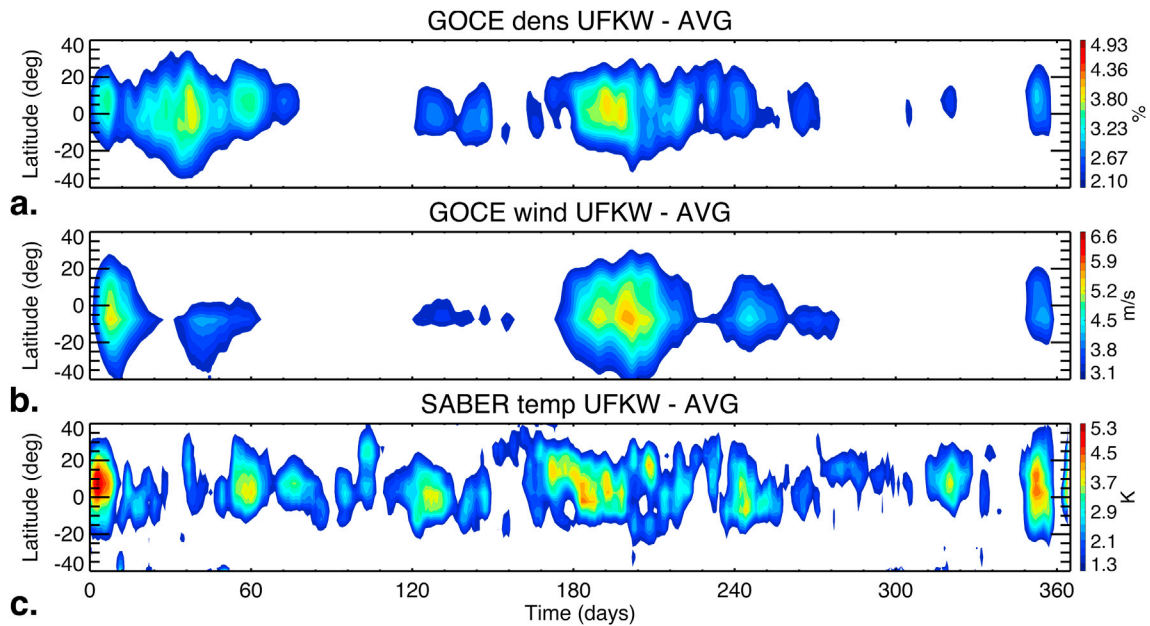


Fig. 5. Similar to Fig. 4, but for the UFKW. Note a significant semi-annual variation with maxima around DOY 1–60 and DOY 170–260 at 260 km, with no identifiable seasonal pattern at 110 km.

important to the local physics of the wave, thus an upward propagating wave entering this region transitions from an exponential growth to an exponential decay in the lower thermosphere. The dependence of χ on λ_z^2 , σ , and ρ is such that the altitude at which the molecular processes dominate increases with vertical wavelength (quadratically), the wave's frequency, and the mean density. [Note that in the above we neglected the effect of zonal mean winds.] This altitude is the 120–130 km height-range for DE3's Kelvin mode and UFKW.

To gain some insights of how waves are affected by dissipation above the peak, Yanowitz 1967 and Lindzen 1968, 1970 define the parameter $\beta = \frac{2\pi H}{\lambda_z}$, where H is the scale height ($H = \frac{kT}{mg}$, T is temperature, k is the Boltzmann constant, m is the mean mass, and g is acceleration due to

Earth's gravity), and obtained analytically the following results: (1) the magnitude of reflection due to inhomogeneities is given by $e^{-\pi\beta}$; (2) for $\beta \leq 2$, wave amplitudes increase roughly as $e^{x/2}$ (where x is in logarithm pressure coordinates) up to the region where $\chi \sim 1$, asymptotically approaching a constant above this level with little or no decrease in amplitude; (3) for $\beta > 2$, wave amplitudes increase roughly as $e^{x/2}$ up to the region where $\chi \sim 1$, but then decrease considerably before asymptotically reaching a constant value. The first symmetric mode of DE3 and the UFKW fall under the third category. Increased solar activity corresponds to higher mean density (i.e., higher χ values) and larger scale heights (i.e., higher β value), which will correspond to higher peak heights and reduced amplitudes in the middle thermosphere.

At higher levels the response is height-independent due to fast vertical diffusion and the height at which this occurs is also dependent on solar activity level. In particular fast vertical diffusion takes hold at a lower height for solar low conditions. The density response above this altitude is such that the hydrostatic law determines how the response increases with height during a given level of solar activity, as well as the dependence of the response at upper levels to solar activity (these are of course related to each other). To understand this behavior one can write the hydrostatic law $\frac{d\rho}{dz} = -\frac{\rho}{H}$, where ρ is density, z is height, and $H = \frac{kT}{Mg}$ is a constant scale height (with k = Boltzmann constant, T = temperature, M = mean mass, g = acceleration due to gravity). A linearized version is $\frac{d\rho_0}{dz} + \frac{d\rho'}{dz} = -\frac{1}{H_0 + H'}$, where subscript zero denotes diurnal mean and primed corresponds to wave perturbation. Hence $\frac{d\rho'}{dz} = -\frac{1}{H_0} \left(\frac{1}{1 + \frac{H'}{H_0}} \right)$,

which for $H' \ll H_0$ can be written as $\frac{d\rho'}{dz} \approx -\frac{1}{H_0} \left(1 - \frac{H'}{H_0} \right)$. Therefore, using the hydrostatic law, one can write the following simplified expression for density perturbations as function of height: $\rho' = \rho'_0 e^{\frac{H'}{H_0}(z-z_0)}$. Higher S10.7 levels correspond to larger scale heights, yielding an inverse relationship between the rate of increase of density perturbation with height and S10.7.

Summarizing, for horizontal winds and temperatures, the mean density determines: (1) the height of the peak (i.e., χ factor); (2) the shape of response above the peak (β factor); (3) height-independent response at higher levels due to fast vertical diffusion [Note that (3) and (2) are related, since fast vertical diffusion takes hold at a lower height during solar minimum]; (4) for density response in the regime of (3), above the hydrostatic law determines how the response increases with height during a given level of solar activity, as well as the dependence of the response at upper levels to solar activity.

3.3.2. SABER and GOCE results

One of the goals of this study is to gain further insight into the effects of solar EUV variations, as embodied in the S10.7 index, on the vertical coupling of DE3 and the UFKW from the lower to the middle thermosphere. To this end, we analyze the temporal-latitude variability of DE3 and UFKW in relation to S10.7 variations, focusing on variations longer than ~ 27 days. To better characterize the impact of solar EUV radiation on vertical coupling, we isolate the symmetric component of DE3. The first symmetric mode of DE3 is a Kelvin wave that is known to propagate high into the thermosphere due to its long vertical wavelength [Oberheide et al., 2011; Forbes et al., 2014]. The first anti-symmetric mode of DE3 can have significant effects on the latitudinal profile of DE3 in the lower thermosphere and impose departures from its otherwise primarily equatorially symmetric structure. The first anti-symmetric mode of DE3 has a vertical wavelength of around 30 km and thus is less likely to vertically propagate to the middle thermosphere compared to the first symmetric mode that has $\lambda_z \sim 56$ km (both estimated by Truskowski et al., 2014 from classical tidal theory for isothermal conditions). Also, the anti-symmetric component can be introduced in-situ by mean winds. Therefore, isolating the symmetric component of DE3 that is known to propagate well into the middle thermosphere is necessary to effectively investigate the impact of solar activity on the vertical coupling.

In order to compare DE3 amplitudes at 110 km with those at 260 km, we convert SABER-derived DE3 temperatures at 110 km to densities using the ratio between the two given by Hough Mode Extensions (HMEs), and perform the same analysis for the UFKW. HMEs represent the global solution to the linearized dynamical equations of the atmosphere for an oscillation of given frequency and zonal wavenumber, taking into account dissipative effects above the forcing region. The perturbation fields (i.e., u, w, v, T, ρ) output from the HMEs maintain internally self-consistent relative amplitude and phase relationships, thus enabling the estimation of DE3 (UFKW) densities from DE3 (UFKW)

temperatures. The HMEs are the same as in Oberheide et al., 2009, computed as detailed by Svoboda et al., 2005 using a stripped-down version of the Global Scale Wave Model (GSWM), calculated for three F10.7 radio flux levels: high (170 sfu), moderate (110 sfu) and low (60 sfu). Oberheide et al., 2009 found strong solar flux dependence in DE3 amplitudes in the thermosphere, with smallest amplitudes for high solar flux and largest for low solar flux. The HME solar flux dependence in the MLT is shown to be small with only a few percent (density, winds) or even less (temperature). Temperature HMEs are found to be the least sensitive to solar cycle effects with a 60% increase from 170 sfu to 60 sfu, while density (almost a factor of 5) and winds (a factor of 2–3) are more affected. [Solar cycle effects are much more pronounced for density as opposed to temperature, since the former reflects a height-integrated response to the former.]

Fig. 6 shows the latitude versus solar flux dependence in the ratio between DE3 temperatures and DE3 densities at 110 km (panel a) and 260 km (panel b), derived by linearly interpolating HMEs for the 3 solar flux levels previously described. As shown in Fig. 6a, at 110 km the ratio is not significantly affected by solar flux or latitude, with values varying from 1.7 for F10.7 ~ 60 to 1.8 for F10.7 ~ 200 , while at 260 km (as shown in Fig. 6b) the ratio has a strong solar flux dependence, with values from 3 for F10.7 ~ 60 to 8 for F10.7 ~ 200 . At both heights the ratios are maxima around the equator and decrease considerably with latitude. We use these ratios to convert DE3 temperatures at 110 km to DE3 density perturbations at the same height, accounting for latitude and solar flux variations. A similar procedure is used for the UFKW, although for this case no solar flux dependence is included (this could introduce errors up to 0.5%). These derived DE3 (UFKW) density perturbations at 110 km can be then effectively compared to the density perturbations at 260 km derived from GOCE measurements.

Fig. 7a displays symmetric DE3 density perturbations calculated around the equator ($\pm 12^\circ$ latitude) as 27-day running means at 110 km (black line) and 260 km (blue line). The red line represents the time evolution of the S10.7 index, also shown as 27-day running mean. We used 27-day means to remove day-to-day variations and reduce noise, while highlighting longer-period (e.g., seasonal) effects. Amplitudes up to 11% (7%) are found at 110 km (260 km), with no noticeable correlation to S10.7 at either heights. One of the issues when investigating the effect of solar radiation on the vertical propagation is separating the effect of decreased amplitudes at 260 km due to less generation at lower heights (i.e., reduced tropospheric latent heat release), from the influence of solar radiation on the coupling. In order to focus on the latter, we

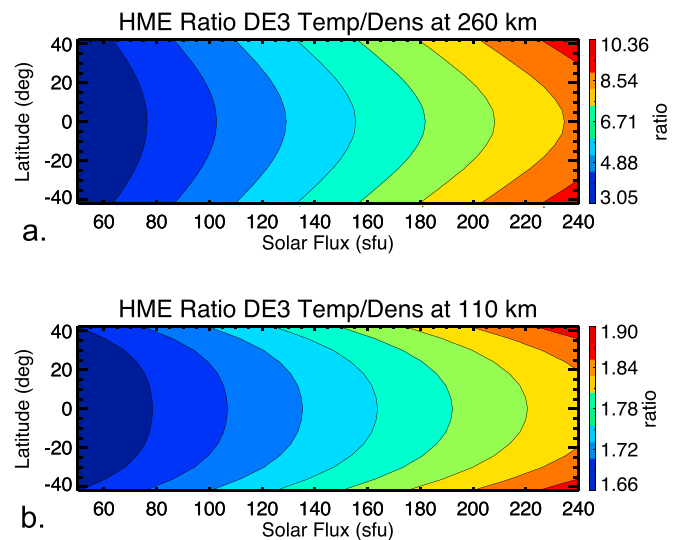


Fig. 6. Ratio between DE3 in temperatures and DE3 densities for the first symmetric mode at 110 km (panel a) and 260 km (panel b), calculated using HMEs, as function of solar flux and latitude.

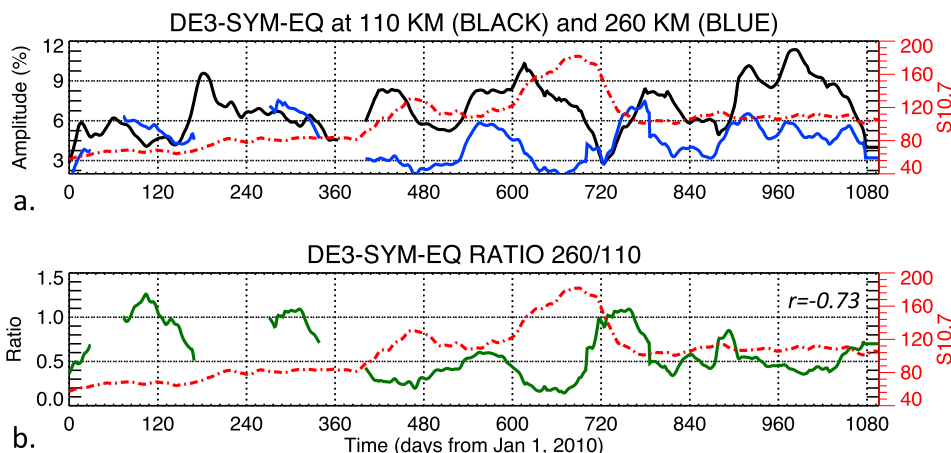


Fig. 7. (a) Symmetric DE3 density perturbations at 110 km (black line) and 260 km (blue line) compared to S10.7 (red dashed-dot line) for 2010–2012. The amplitudes refer to 27-day running means and are averaged around the equator ($\pm 12^\circ$ latitude). DE3 temperatures at 110 km are converted to DE3 densities using the HME ratios shown in Fig. 6. (b) Ratios between symmetric DE3 densities at 260 km and 110 km (green line), compared to S10.7 variability (red line). Significant anti-correlation is found between the ratios and S10.7 with $r = -0.73$ over the 3-year period. (For interpretation of the references to colour in this figure legend, the reader is referred to the web version of this article.)

analyze the time series of the ratio between DE3 densities at 110 km and those at 260 km, as shown by the green line in Fig. 7b. Although DE3 presents no clear correlation with S10.7 at 110 km or 260 km, the ratio between the DE3 at the two heights shows significant anti-correlation with the solar EUV index ($r = -0.73$). This result agrees with the physics underlined in Section 3.3.1. Increased (decreased) solar activity corresponds to higher (lower) mean density and larger (smaller) scale heights, which translates to higher (lower) peak heights and reduced (increased) amplitudes around 200 km. Above about 200 km, where fast vertical diffusion occurs, the hydrostatic law determines how the density response increases with height for a given level of solar activity. Higher (lower) S10.7 levels translate to larger (smaller) scale heights, thus a reduction (increase) in the rate of growth of density perturbation with height, resulting in smaller (larger) amplitudes in the middle thermosphere (i.e., 260 km). Both of these effects contribute to produce reduced density perturbations in the middle thermosphere for higher solar activity levels, thus yielding the observed anti-correlation between the DE3 density ratios and S10.7 values.

In Fig. 8, the ratios (i.e., 260 km over 110 km) of symmetric DE3 density perturbations as function of latitude and S10.7 level calculated using SABER and GOCE data (panel a) are compared with the ones calculated from HMEs (panel b). Fig. 8c shows the scatter plot of S10.7 versus DE3 ratios at the equator and the linear fit used to derive Fig. 8a. The similarities between the HME predictions and the SABER-GOCE observations are compelling. Examining Fig. 8, one can see the inverse relationship between S10.7 and the DE3 ratios, but also evidence of latitudinal broadening with height. The broadening of latitude structures with height is evidenced by increasing ratios with latitude for fixed levels of solar activity. This characteristic is attributable to the effect of dissipation (see discussions in sections 3.1 and 3.2). The ratios are comprised between 0.1 and 0.8 for S10.7 ranging from 60 to 200 and are higher for lower solar activity levels.

Fig. 9 presents the altitude profile of symmetric DE3 density perturbations (panel a) and the ratios normalized to 110 km (panel b) for three solar flux levels: 70 sfu, 110 sfu, and 170 sfu, as output from the HMEs (same as Oberheide et al., 2009). As shown in Fig. 9, DE3 density perturbations reach a maximum of about 16.5% around 120 km (where $\chi \approx 1$) and then decrease exponentially (according to the factor β) before increasing again above around 200 km (according to the hydrostatic law). The amplitude of the peak is not very sensitive to the solar flux level and the height of the peak only slightly; however, the profile shape above the peak varies significantly with solar flux level, such that higher amplitudes are achieved in the middle-upper thermosphere (i.e., >200 km) for lower F10.7 values. As previously discussed, this phenomenon is due

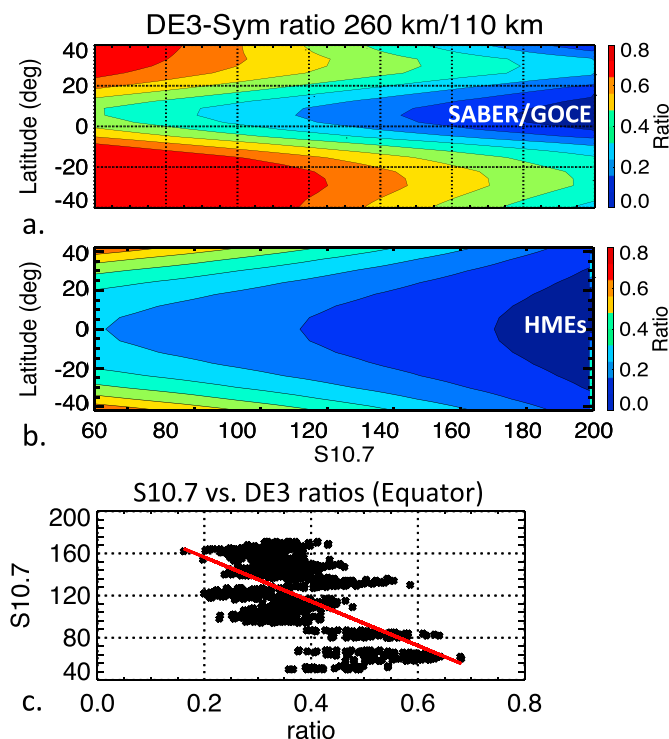


Fig. 8. Ratios of symmetric DE3 density perturbations as function of latitude and S10.7 level calculated linearly fitting S10.7 and the ratios from SABER and GOCE data (panel a) and from HMEs (panel b). Strong similarities between HMEs and SABER-GOCE observations, with ratios comprised between 0.1 and 0.8 for S10.7 ranging from 60 to 200. Note the inverse relationship between S10.7 and the DE3 ratios and the latitudinal broadening with height due to the effect of dissipation. Panel c shows the scatter plot of S10.7 versus DE3 ratios at the equator and the linear fit used to derive the ratios in panel a.

to the combined effect of dissipation above the peak (i.e., parameter β), and the hydrostatic law above about 200 km. Fig. 9 also shows the vertical profile of symmetric DE3 temperatures from HMEs (dot-dashed lines). Note that temperatures reach asymptotic values (i.e., the response is height-independent) above about 200 km, where density perturbations increase according to the hydrostatic law. Also note that in the middle thermosphere the temperature ratios are not as sensitive to solar activity level as the density perturbations and do not increase considerably with height above about 300 km.

In addition to displaying the vertical profiles of DE3 from HMEs,

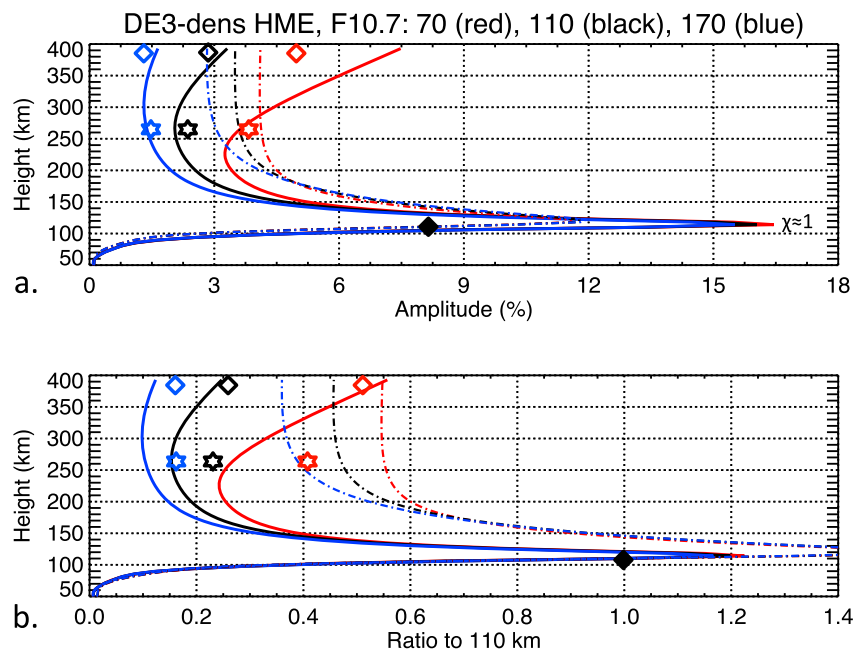


Fig. 9. Altitude profile of DE3 density perturbations (panel a) and ratios normalized to 110 km (panel b) for three solar flux levels: 70 sfu (red line), 110 sfu (black line), and 170 sfu (blue line), as output from the HMEs. The dot-dashed line shows DE3 temperatures (note: the amplitudes are divided by 3) and ratios. The height and amplitude of the peak ($\chi \approx 1$) are not very sensitive to the solar flux level, although the profile shape above the peak varies significantly with solar flux level. Also shown are 120-day mean density perturbations from CHAMP at ~ 400 km (empty squares), GOCE at ~ 260 km (empty stars), and SABER at ~ 110 km (full squares), with red referring to low solar activity (i.e., 70 sfu), black to medium solar activity (i.e., 110 sfu), and blue refers to high solar activity (i.e., 170 sfu). Note the general agreement between the HME predictions and the observations, and the strong effect of solar activity level. (For interpretation of the references to colour in this figure legend, the reader is referred to the web version of this article.)

Fig. 9a also shows the density perturbations calculated from CHAMP at ~ 400 km (empty squares), GOCE at ~ 260 km (empty stars), and SABER at ~ 110 km (full squares), while **Fig. 9b** shows the ratios of these perturbations to the values at 110 km. Similar to the HME lines, red refers to low solar activity (i.e., 70 sfu), black refers to medium solar activity (i.e., 110 sfu), and blue refers to high solar activity (i.e., 170 sfu). The density perturbations for CHAMP at 400 km are derived from Oberheide et al., 2009 and refer to 120-day means. For consistency to the CHAMP values, the SABER and GOCE amplitudes shown **Fig. 9** are also calculated with respect to 120-day running means. Note the general agreement between the HME predictions and the observations, and the strong effect of solar activity on the vertical evolution of DE3 density perturbations in the middle and upper thermosphere. As previously discussed, this effect becomes greater as the altitudes become higher. For instance, the perturbations at 260 km are 1.5% for solar low, 2.4% for solar medium, and 3.6% for solar high conditions, thus a $\sim 250\%$ increase from solar low to solar high. While at 400 km these values are 1.4%, 2.9%, and 5.0% yielding a $\sim 350\%$ increase from solar low to solar high. Also note that the height and amplitude of the peak does not depend appreciably on the level of solar activity, as predicted by HMEs and demonstrated by SABER observations at 110 km.

Fig. 10 shows the temporal evolution of equatorial density perturbations (panel a) and ratios (panel b) for the UFKW at 110 km and 260 km. UFKW temperatures at 110 km are converted to density perturbations at the same height using the ratio between the two given by HMEs for a 3-day Kelvin wave with $s = -1$. Similar to DE3 (i.e., **Fig. 7b**), the UFKW ratios also show anti-correlation with the S10.7 index ($r = -0.62$). Lower anti-correlation for the UFKW than DE3 is expected due to the larger number of differences between the latitude-temporal structures at 110 km and those at 260 km (see section 3.1). **Fig. 11a** shows the latitude-S10.7 dependency in the ratios for the UFKW, while **Fig. 11b** shows the scatter plot of S10.7 versus UFKW ratios at the equator, similar to what is presented in **Fig. 8** for DE3. Also in this case the ratios increase with latitude due to the effect of latitudinal broadening induced by dissipation and are inversely related to the level of solar activity, i.e., higher (lower) S10.7 values correspond to smaller

(larger) ratios.

4. Conclusions

It is now well accepted that a few global-scale waves from the tropical wave spectrum preferentially propagate into the thermosphere, where they modulate neutral and plasma densities, deposit their momentum and modify the mean circulation. While considerable improvements have been made on the understanding of MLT dynamics, driven in part by the development and deployment of new instruments and techniques, relatively little is known about the coupling of waves in the 120–300 km thermospheric gap between satellite remote-sensing and in-situ wave diagnostics. It is becoming increasingly evident that background atmospheric conditions in this region filter the tropical wave spectrum and modulate it into the thermosphere.

In this work, TIMED-SABER temperatures at 110 km and GOCE neutral densities and cross-track winds around 260 km are employed to reveal and investigate the vertical coupling of two of the more prominent and well-established tropical Kelvin waves: the UFKW and DE3. The analysis is performed at low-to mid-latitudes ($\pm 45^\circ$) for solar low and geomagnetic quiet conditions during 2010–2012. The main findings of this study can be summarized as follows:

- DE3 maximizes within about $\pm 15^\circ$ latitude both at 110 km and 260 km, and can be detected in the $\pm 30^\circ$ latitude range, while the UFKW shows the largest amplitudes within about $\pm 25^\circ$ latitude at 110 km and possesses non-negligible amplitudes up to $\pm 40^\circ$ latitude at 260 km. Amplitudes larger than 15 K are found in DE3 and UFKW temperatures at 110 km and up to 8% (10 m/s) in DE3 and UFKW densities (winds) at 260 km. Both waves are shown to vertically propagate in this height regime and demonstrate evidence of latitudinal broadening and filtering of the latitude structures with height, likely induced by the combined effect of dissipation and zonal mean winds.
- The seasonal course of DE3 is dominated by a primary maximum of ~ 16 K at 110 km and $\sim 6\%/ \sim 10$ m/s at 260 km around

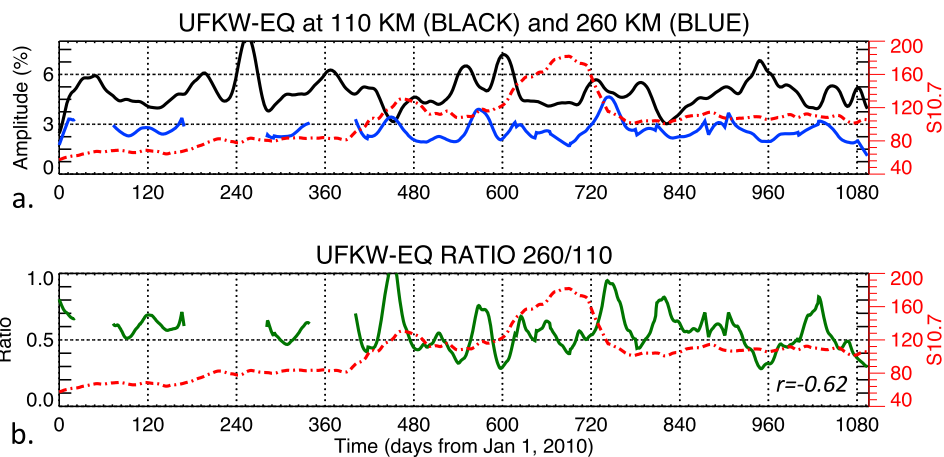


Fig. 10. Same as Fig. 8, but for the UFKW. Anti-correlation between the UFKW ratios and S10.7 is found with $r = -0.62$ for the 3-year period calculated around the equator ($\pm 12^\circ$ latitude). Lower correlation for the UFKW can be expected and is likely due to less coherence in the variability between 110 km and 260 km for this wave compared to DE3, as discussed for Fig. 3.

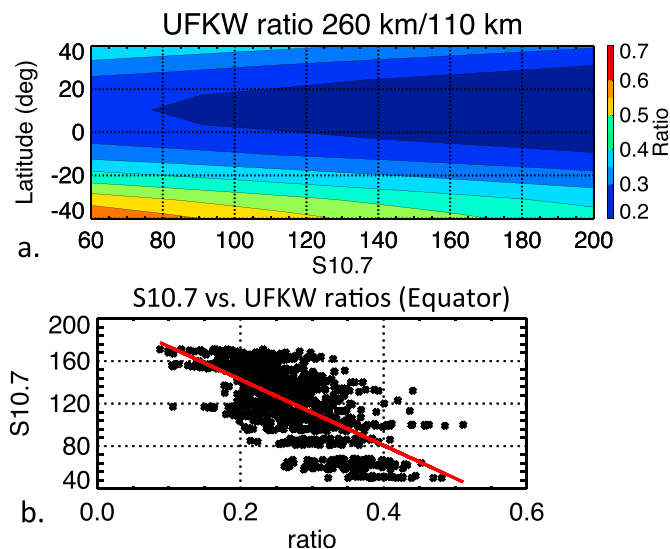


Fig. 11. Same as Fig. 9a, but for the UFKW. Similar conclusions as for DE3, with inverse correlation between the ratios and S10.7 as well as latitudinal broadening with height due to dissipation.

August–September and a secondary maximum of ~ 8 K at 110 km and ~ 6 m/s/ $\sim 3\%$ at 260 km during January–March. The UFKW shows weak seasonal dependence at 110 km, but a strong semi-annual oscillation at 260 km, probably due to filtering associated with the effect of zonal mean winds, with maxima of $\sim 4\%$ and ~ 6 m/s around January–February and July–August.

- Anti-correlation between the vertical response of DE3 and UFKW and solar activity level is established. Reduced (increased) amplitudes in the middle thermosphere are found for increased (decreased) solar activity levels. This response is explained as due to the effect of molecular dissipation below ~ 200 km and the hydrostatic law above ~ 200 km. This finding points to the importance played by solar activity level on the vertical coupling of waves in the thermosphere.

Acknowledgements

This work was supported under grant NNX12AD26G from NASA to the University of Colorado under the U.S. Participating Investigator (USPI) Program for the GOCE Mission, and through subaward 75900816 to Utah State University. TIMED-SABER data can be freely accessed at

<http://saber.gats-inc.com/data.php>, while GOCE data can be freely accessed at <https://earth.esa.int/web/guest/-/goce-data-access-7219>, logging in the GOCE Virtual Online Archive (login credentials may be obtained by registering to the ESA portal).

Bibliography

Andrews, D.G., Holton, J.R., Leovy, C.B., 1987. Middle Atmospheric Dynamics. Academic Press, p. 489.

Bruinsma, S.L., Doornbos, E., Bowman, B.R., 2014. Validation of GOCE densities and thermosphere model evaluation. *Adv. Space Res.* 54, 576–585.

Bruinsma, S.L., Förste, C., Abrikosov, O., Marty, J.-C., Rio, M.-H., Mulet, S., Bonvalot, S., 2013. The new ESA satellite-only gravity field model via the direct approach. *Geophys. Res. Lett.* 40, 3607–3612.

Bowman, B.R., Tobiska, W.K., Marcos, F., Valladares, C., 2008. The JB2006 empirical thermospheric density model. *J. Atmos. Sol. Terr. Phys.* 70, 774–793.

Chapman, S., Lindzen, R.S., 1970. Atmospheric Tides. D. Reidel Press, Dordrecht, Holland.

Doornbos, E., 2016. Air Density and Wind Retrieval Using GOCE Data, European Space Agency (ESA) AO/1–6367/10/NL/AF. Version 1.5 Data Set User Manual.

Doornbos, E., Bruinsma, S.L., Fritsche, B., Koppenwallner, G., Visser, P., van den IJssel, J., de Teixeira de Encarnacao, J., 2014. Air Density and Wind Retrieval Using GOCE Data. Final Rep. European Space Agency (ESA) Contract 4000102847/NL/EL.

Doornbos, E., Visser, P., Koppenwallner, G., Fritsche, B., 2013. Air Density and Wind Retrieval Using GOCE Data. ESA AO/1–6367/10/NL/AF, Algorithm Theoretical Basis Document 1.1.

Drinkwater, M.R., Floberghagen, R., Haagmans, R., Muzi, D., Popescu, A., 2003. GOCE: ESAs First Earth Explorer Core Mission, vol. 18. Kluwer Academic Publishers, pp. 419–432.

England, S.L., Immel, T.J., Huba, J.D., Hagan, M.E., Maute, A., DeMajistre, R., 2010. Modeling of multiple effects of atmospheric tides on the ionosphere: an examination of possible coupling mechanisms responsible for the longitudinal structure of the equatorial ionosphere. *J. Geophys. Res.* 115, A05308.

Forbes, J.M., 2000. Wave coupling between the lower and upper atmosphere: Case study of an ultra-fast kelvin wave. *J. Atmos. Sol. Terr. Phys.* 62, 1603–1621.

Forbes, J.M., Zhang, X., Bruinsma, S.L., 2014. New perspectives on thermosphere tides - 2. penetration to the upper thermosphere. *Earth, Planets Space* 66, 122.

Forbes, J.M., Bruinsma, S.L., Zhang, X., Oberheide, J., 2009. Surface-exosphere coupling due to thermal tides. *Geophys. Res. Lett.* 36, L15812.

Forbes, J.M., Bruinsma, S.L., Miyoshi, Y., Fujiwa, H., 2008. A solar terminator wave in thermosphere neutral densities measured by the CHAMP satellite. *Geophys. Res. Lett.* 35.

Forbes, J.M., Hagan, M., Miyahara, S., Miyoshi, Y., Zhang, X., 2003. Diurnal nonmigrating tides in the tropical lower thermosphere. *Earth, Planets Space* 55, 419–426.

Forbes, J.M., Vincent, R.A., 1989. Effects of mean winds and dissipation on the diurnal propagating tide: an analytic approach. *Planet. Space Sci.* 37, 197–209.

Forbes, J.M., Hagan, M.E., 1982. Thermospheric extensions of the classical expansion functions for semidiurnal tides. *J. Geophys. Res.* 87, 5253–5259.

Forbes, J.M., Garrett, H.B., 1979. The solar cycle variability of diurnal and semidiurnal thermospheric temperatures. *J. Geophys. Res.* 84, 1947–1949.

Gasperini, F., Forbes, J.M., Doornbos, E.N., Bruinsma, S.L., 2015. Wave coupling between the lower and middle thermosphere as viewed from TIMED and GOCE. *J. Geophys. Res.* 120, 5788–5804.

García-Comas, M., González-Galindo, F., Funke, B., Gardini, A., Jurado-Navarro, A., López-Puertas, M., Ward, W.E., 2016. MIPAS observations of longitudinal oscillations in the mesosphere and the lower thermosphere: climatology of odd-parity daily

- frequency modes. *Atmos. Chem. Phys.* 16, 11019–11041. <http://dx.doi.org/10.5194/acp-16-11019-2016>.
- Gu, S.Y., Dou, X., Lei, J., Li, T., Luan, X., Wan, W., Russell III, J.M., 2014. Ionospheric response to the ultrafast Kelvin wave in the MLT region. *J. Geophys. Res.* 119, 1369–1380.
- Hagan, M.E., Maute, A., Roble, R.G., 2009. Tropospheric tidal effects on the middle and upper atmosphere. *J. Geophys. Res.* 114, A01302.
- Häusler, K., Hagan, M.E., Forbes, J.M., Zhang, X., Doornbos, E., Bruinsma, S., Lu, G., 2015. Intraannual variability of tides in the thermosphere from model simulations and in situ satellite observations. *J. Geophys. Res. Space Phys.* 120, 751–765. <http://dx.doi.org/10.1002/2014JA020579>.
- He, M., Liu, L., Wan, W., Wei, Y., 2011. Strong evidence for couplings between the ionospheric wave structure and atmospheric tides. *Geophys. Res. Lett.* 38, L14101.
- Hitchman, M., Leovy, C., 1985. Diurnal tide in the equatorial middle atmosphere as seen in LIMS temperatures. *Amer. Meteor. Soc.* 42, 557–561.
- Immel, T.J., Sagawa, E., England, S.L., Henderson, S.B., Hagan, M.E., Mende, S.B., Frey, H.U., Swenson, C.M., Paxton, L.J., 2006. Control of equatorial ionospheric morphology by atmospheric tides. *Geophys. Res. Lett.* 33.
- Jiang, G., Wang, W., Xu, J., Yue, J., Burns, A.G., Lei, J., Mlynczak, M.G., Russell III, J.M., 2014. Responses of the lower thermospheric temperature to the 9 day and 13.5 day oscillations of recurrent geomagnetic activity. *J. Geophys. Res.* 119, 4841–4859.
- Jin, H., Miyoshi, Y., Fujiwara, H., Shinagawa, H., 2008. Electrodynamic of the formation of ionospheric wave number 4 longitudinal structure. *J. Geophys. Res.* 113, A09307.
- Jones Jr., M., Forbes, J.M., Hagan, M.E., 2014. Tidal-induced net transport effects on the oxygen distribution in the thermosphere. *Geophys. Res. Lett.* 41, G060698.
- Jones Jr., M., Forbes, J.M., Hagan, M.E., Maute, A., 2013. Non-migrating tides in the ionosphere-thermosphere: in situ versus tropospheric sources. *J. Geophys. Res.* 118.
- Kil, H., Talaat, E.R., Oh, S.J., Paxton, L.J., England, S.L., Su, S.J., 2008. Wave structures of the plasma density and vertical $E \times B$ drift in low-latitude F region. *J. Geophys. Res.* 113, A09312.
- Kil, H., Oh, S.-J., Kelley, M.C., Paxton, L.J., England, S.L., Talaat, E., Min, K.-W., Su, S.-Y., 2007. Longitudinal structure of the vertical $E \times B$ drift and ion density seen from ROCSAT-1. *Geophys. Res. Lett.* 34, L14110.
- Lei, J., Thayer, J.P., Forbes, J.M., Sutton, E.K., Nerem, R.S., 2008. Rotating solar coronal holes and periodic modulation of the upper atmosphere. *Geophys. Res. Lett.* 35, L10109.
- Leonard, J.M., Forbes, J.M., Born, G.H., 2012. Impact of tidal density variability on orbital and reentry predictions. *Space Weather.* 10, S12003. <http://dx.doi.org/10.1029/2012SW000842>.
- Lieberman, R.S., 1991. Nonmigrating diurnal tides in the equatorial middle atmosphere. *J. Atmos. Sci.* 48, 1112–1123.
- Lindzen, R.S., 1970. Internal equatorial planetary scale waves in shear flow. *J. Atmos. Sci.* 27, 394–407.
- Lindzen, R.S., 1968. Vertically propagating waves in an atmosphere with Newtonian cooling inversely proportional to density. *Can. J. Phys.* 46, 1835–1840.
- Lindzen, R.S., McKenzie, D.J., 1967. Tidal theory with Newtonian cooling. *Pure Appl. Geophys.* 64, 90–96.
- Liu, H., Watanabe, S., 2008. Seasonal variation of the longitudinal structure of the equatorial ionosphere: does it reflect tidal influences from below? *J. Geophys. Res.* 113, A08315.
- Liu, H., Stolle, C., Förster, M., Watanabe, S., 2007. Solar activity dependence of the electron density at 400 km at equatorial and low latitudes observed by CHAMP. *J. Geophys. Res.* 112, A11311.
- Mukhtarov, P., Pancheva, D., 2011. Global ionospheric response to nonmigrating DE3 and DE2 tides forced from below. *J. Geophys. Res.* 116, A05323.
- Oberheide, J., Forbes, J.M., Zhang, X., Bruinsma, S.L., 2011. Wave-driven variability in the ionosphere-thermosphere-mesosphere system from TIMED observations: what contributes to the wave 4. *J. Geophys. Res.* 116, A01306.
- Oberheide, J., Forbes, J.M., Wu, Q., Häusler, K., Bruinsma, S.L., 2009. Tropospheric tides from 80 to 400 km: propagation, interannual variability, and solar cycle effects. *J. Geophys. Res.* 114.
- Oberheide, J., Forbes, J.M., 2008. Tidal propagation of deep tropical cloud signatures into the thermosphere from TIMED observations. *Geophys. Res. Lett.* 35.
- Oberheide, J., Gusev, O.A., 2002. Observation of migrating and nonmigrating diurnal tides in the equatorial lower thermosphere. *Geophys. Res. Lett.* 29 (24), 2167.
- Oberheide, J., Hagan, M.E., Ward, W.E., Riese, M., Offermann, D., 2000. Modeling the diurnal tide for the cryogenic infrared spectrometers and telescopes for the atmosphere (CRISTA) 1 time period. *J. Geophys. Res.* 105, 24917–24929.
- Pancheva, D., Mukhtarov, P., 2010. Strong evidence for the tidal control on the longitudinal structure of the ionospheric F-region. *Geophys. Res. Lett.* 37, L14105.
- Salby, M.L., Hartmann, D.L., Bailey, P.L., Gille, J.C., 1984. Evidence for equatorial Kelvin modes in Nimbus-7 LIMS. *J. Atmos. Sci.* 41, 220–235.
- Svoboda, A.A., Forbes, J.M., Miyahara, S., 2005. A space-based climatology of MLT winds, temperatures and densities from UARS wind measurements. *J. Atmos. Solar-Terr. Phys.* 67, 1533–1543.
- Tobiska, W.K., Bouwer, S., Bowman, B.R., 2008. The development of new solar indices for use in thermospheric density modeling. *J. Atmos. Sol. Terr. Phys.* 70, 803–819.
- Truskowski, A.O., Forbes, J.M., Zhang, X., Palo, S.E., 2014. New perspectives on thermosphere tides: 1. lower thermosphere spectra and seasonal-latitudinal structures. *Earth, Planets Space* 136 (66), 1.
- Wheeler, M., Kiladis, G.N., 1999. Convectively coupled equatorial waves: analysis of clouds and temperature in the wavenumber-frequency domain. *J. Atmos. Sci.* 56, 374–399.
- Yanowitz, M., 1967. Effect of viscosity on gravity waves and the upper boundary condition. *J. Fluid Mech.* 29, 209–231.
- Zhang, X., Forbes, J.M., Hagan, M.E., Russell III, J.M., Palo, S.E., Mertens, C.J., Mlynczak, M.G., 2006. Monthly tidal temperatures 20–120 km from TIMED/SABER. *J. Geophys. Res.* 111, A10S08.